AGU
ADVANCING EARTH AND SPACE SCIENCE

Geophysical Research Letters®

Key Points:
- Decameter scale irregularities are positively correlated with intermediate scale density gradients irrespective of directions
- Decameter scale ionospheric irregularities are enhanced at the dayside cusp and dawnside auroral region
- These irregularities are likely caused by auroral particle precipitation/ plasma dynamics

Statistical Distribution of Decameter Scale (50 m) Ionospheric Irregularities at High Latitudes

Yaqi Jin[1] , Lasse B. N. Clausen[1] , Andres Spicher[2] , Magnus F. Ivarsen[1] , Yongliang Zhang[3] , Wojciech J. Miloch[1] , and Jøran I. Moen[1,4]

[1]Department of Physics, University of Oslo, Oslo, Norway, [2]Department of Physics and Technology, The Arctic University of Norway, Tromsø, Norway, [3]The Johns Hopkins University Applied Physics Laboratory, Laurel, MD, USA, [4]Arctic Geophysics, University Centre in Svalbard, Longyearbyen, Norway

Abstract We present a study of decameter scale ionospheric irregularities using in-situ electron density data from the NorSat-1 satellite. During the current period of low solar activity, NorSat-1 frequently observes significant plasma irregularities from several 10 s km down to several decameter. These are often observed near the dayside cusp and dawnside auroral zone. The decameter-scale irregularities are positively correlated with intermediate-scale (10 km) density gradients, for both negative and positive gradients encountered by the satellite. The statistical distribution of electron density over two winter months in the northern hemisphere along NorSat-1 orbits, shows significant density increases in the cusp ionosphere (75°–80° Magnetic LATitude) and in regions near the dawnside auroral oval. Intermediate scale density gradients and small-scale irregularities are clearly associated with these density enhancements. We postulate that these density enhancements and irregularities are due to auroral particle precipitation/plasma dynamics.

Plain Language Summary The polar ionosphere is often irregular and turbulent with significant plasma structures. As a result, the satellite-based navigation and communication systems that rely on trans-ionospheric radio signals can be severely affected. In the present study, we take advantage of the high-resolution electron density observations of a polar orbiting satellite to address plasma structures at several 10 s of meters that are responsible for scattering of High Frequency radar signals. The statistical results indicate that enhanced decameter scale structures are often located within the auroral region during the period of low solar activity. This finding highlights the auroral dynamics in creating plasma turbulence at high latitudes.

1. Introduction

Plasma irregularities and turbulence are frequently observed in the polar ionosphere. Ionospheric irregularities span a wide range in spatial scales, from 10s of km down to meter scales (Tsunoda, 1988 and references therein). In this study, we define large-scale structures to have wavelengths $\lambda \geq 100$ km, intermediate scale as $1 < \lambda < 100$ km, and small scale as $\lambda \leq 1$ km. The small-scale irregularities at decameter scales have received much attention due to the backscatter of radio signals from high frequency (HF) radars (e.g., Baker et al., 1986). For the Super Dual Auroral Radar Network (SuperDARN) HF radars operating at frequencies near 10 MHz, the Bragg scale is around 15 m (Moen et al., 2012). Though the HF backscatter has been observed very early, the first in-situ measurements of HF echoing targets were achieved by the ICI-2 sounding rocket (Moen et al., 2012). Moen et al. (2012) presented a case study to test the role of Gradient Drift Instability (GDI) in creating decameter scale irregularities. Later on, Spicher et al. (2016) presented the case of flow shears using data from the ICI-3 sounding rocket. It has been found that the particle precipitation did not directly generate small-scale plasma irregularities (Moen et al., 2012). Instead the soft particle precipitation in the cusp ionosphere initiates/modulates intermediate-scale density enhancements that range from several km to several 10 s km (Kelley et al., 1982; Labelle et al., 1989). The GDI can then operate on the gradients of these edges to create decameter-scale plasma irregularities. This scenario is consistent with the hypothesis of Kelley et al. (1982).

Statistical distributions of decameter scale irregularities have been obtained from the coherent echo occurrence of HF radars (e.g., Ghezelbash et al., 2014; Ruohoniemi & Greenwald, 1997). However, a number

of propagation factors can affect the detection of ionospheric irregularities by HF radars (e.g., Ghezelbash et al., 2014; Milan et al., 1997). To name a few, this includes the requirement of orthogonality condition for the HF radio waves, the D region absorption, the quality of ground surface for $1\frac{1}{2}$ hop signals and strong ground scatter signals. For the in-situ techniques, only occasional sounding rockets and special burst modes (of limited time) applied to instruments on dedicated satellite missions could directly measure electron density variations down to decameter scales (Moen et al., 2012; Villain et al., 1986). Due to a lack of high-resolution in-situ observations of ionospheric irregularities, such statistical study of decameter scale irregularities in the polar ionosphere has not been presented yet. The NorSat-1 satellite is able to continuously measure the ionospheric electron density at a high sampling rate (up to 1 kHz, Hoang et al., 2018). In this study, we will construct the spatial distribution of decameter scale irregularities in the polar ionosphere based on in-situ data from the NorSat-1 satellite.

2. Instrumentation

NorSat-1 is the first Norwegian scientific satellite, which was launched on July 14, 2017 into a polar orbit at approximately 600 km altitude (Hoang et al., 2018). NorSat-1 is a multi-payload micro-satellite (~16 kg, 23 × 39 × 44 cm) that is operated by the Norwegian Space Center. The Norsat-1 satellite is equipped with the multi-needle Langmuir probe (m-NLP) system developed at the University of Oslo (UiO) (Bekkeng et al., 2010; Jacobsen et al., 2010). The m-NLP onboard the NorSat-1 satellite consists of four needle Langmuir probes biased at different voltages that collect currents at high sampling rates (up to 1 kHz). This makes it suitable for studying the small-scale ionospheric electron density irregularities down to a few decameters assuming the satellite speed of ~7.5 km/s. We use the currents from probes #2, #3, and #4 to derive the absolute electron density (Hoang et al., 2018). Due to the issues related to spacecraft charging in the southern hemisphere (Ivarsen et al., 2019), we will only use data from the Northern Hemisphere in this study.

To support our analysis, we also use the auroral images from the Defense Meteorological Satellite Program (DMSP) spacecraft. Both DMSP F17 and F18 carry the Special Sensor Ultraviolet Spectrographic Imager (SSUSI), which takes auroral observations at five wavelengths in the far ultraviolet range (115–180 nm) with high spatial resolution (7–9 km at nadir) by scanning across the track of the orbit every 15 s (Paxton et al., 2001). In addition, we also use the ground-based GPS total electron content (TEC) map. The TEC data, in bins of 1° × 1° in geographic latitude and longitude with time resolution of 5 min, are obtained from the Madrigal database (Rideout & Coster, 2006).

3. Results

3.1. Event on November 30, 2017

The NorSat-1 satellite flies in a quasi-Sun-synchronous orbit in the noon-midnight direction and visits the noontime aurora (cusp) very often. We will first present a pass through the noontime aurora. Figure 1a presents the auroral image at Lyman-Birge-Hopfield long (LBHL) band from DMSP F18. The image is presented in Magnetic LATitude (MLAT)/Magnetic Local Time (MLT) coordinates, where the Sun is toward the top and dawn in on the right. The orbit of DMSP F18 is presented in Figure 1a as a black segment with timestamps annotated. Though the image is noisy, the dayside aurora is clearly visible. To assist the analysis, the Feldstein auroral oval is shown as magenta circle for $Q = 3$ (Holzworth & Meng, 1975). The LBHL auroral oval is obviously thicker than the Feldstein auroral oval. However, around the time sector where NorSat-1 intersected the aurora, the equatorward boundary of the Feldstein auroral oval roughly matches with the LBHL auroral image.

The NorSat-1 satellite crossed the area about ~30 min later with its orbit presented as a red segment. In Figure 1b, the GPS TEC map presents the background ionospheric condition. As the solar terminator (gray line) was too equatorward of the dayside aurora, there was no evident formation of the polar cap patches as presented in other studies (cf., Figure 1b). Figure 1c presents the electron density from the m-NLP instrument at a resolution of 500 Hz. The electron density is derived from the currents collected from the three probes with highest potentials, referred to as probes #2, #3, and #4. The probes are positively biased to 6,
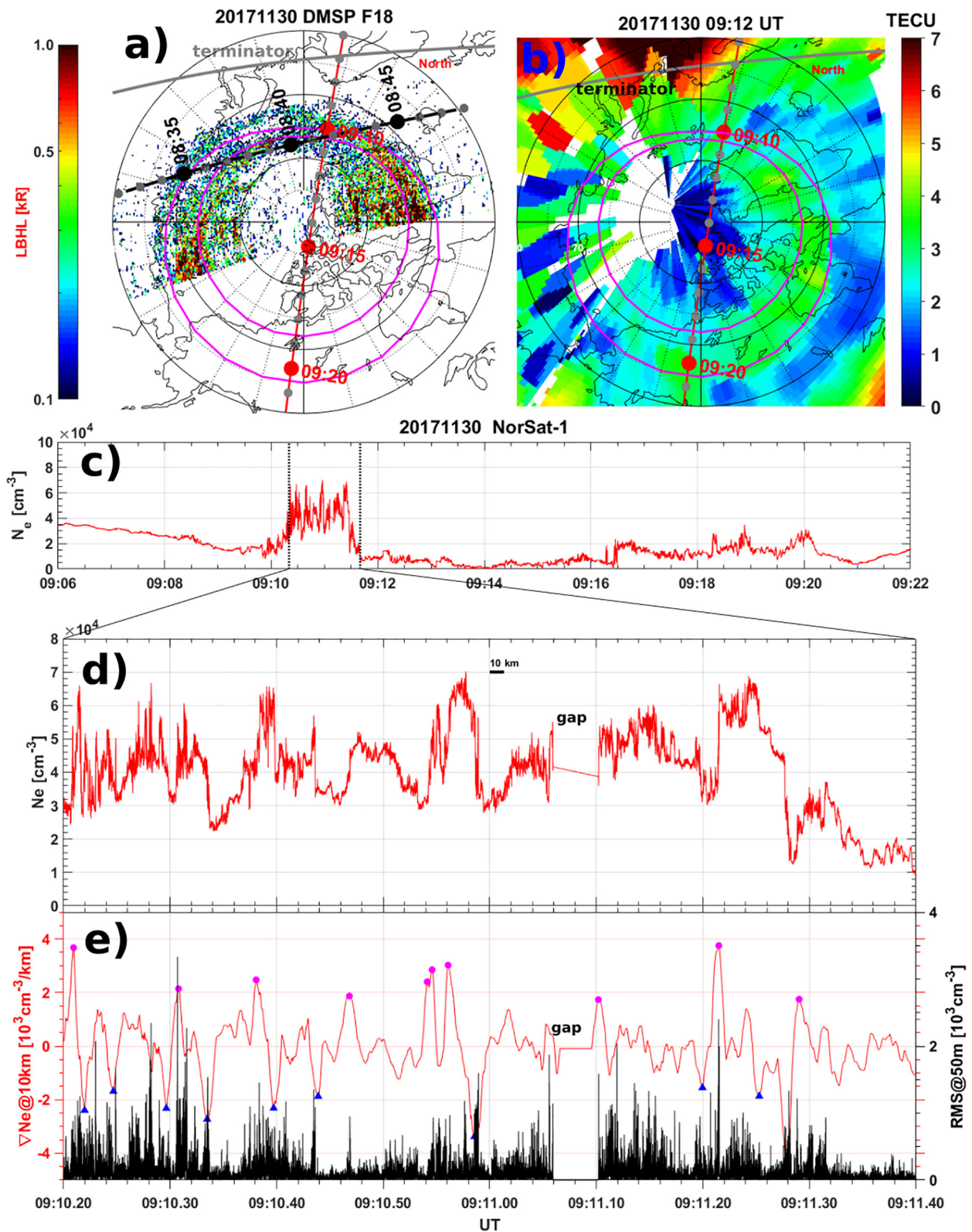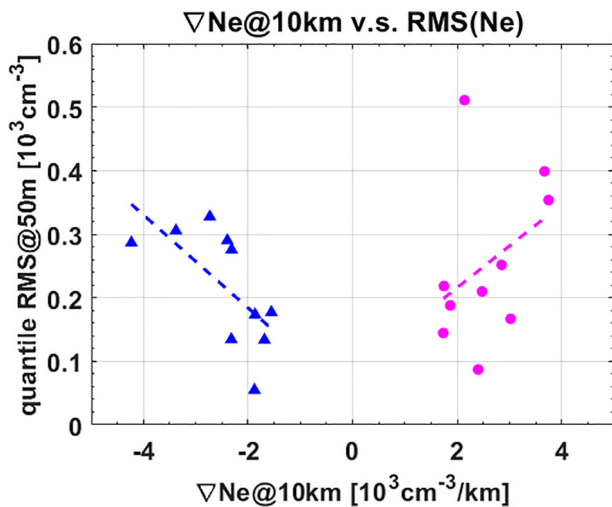
Figure 1.

Figure 2. The relation between small-scale density fluctuations and intermediate-scale density gradients. The gradients are chosen from Figure 1e. The dashed lines show the linear regression. See text for more details.

8, and 10 V, respectively. One can see a clear density enhancement from below 2×10^4 cm^{-3} to above 6×10^4 cm^{-3} between 9:10 and 9:11.40 UT in Figure 1c. This density enhancement roughly matches the noontime auroral oval.

To show the fine-scale structures in the density enhancement, we expand the view of electron density in Figure 1d. The expanded view indicates that there are a few intermediate-scale density enhancements with scale sizes of about 10–50 km (the spatial scale of 10 km is indicated in the middle of Figure 1d). These intermediate-scale structures are likely created by soft particle precipitation in the cusp region. Small-scale (sub-km scale) density fluctuations are observed at the edges and in the middle of these intermediate-scale enhancements (Figure 1d).

Figure 1e shows the density fluctuations in terms of root mean square (RMS) of ΔNe in 50 m, where ΔNe $= N_e - N_{e,smooth}$, and $N_{e,smooth}$ is the smooth electron density in a 50 m running window. By assuming a stationary plasma condition, the spatial scales can be converted from measurements along the orbit by using $\lambda = \Delta t \cdot v_{sc}$, where Δt is the time of measurements, λ is the considered spatial scale, and v_{sc} is the satellite of 7.5 km/s. To better visualize the relation between small-scale density fluctuations and the intermediate-scale density gradients, Figure 1e also displays the intermediate-scale density gradient (∇Ne) by using a linear regression over 10 km (667 data points for the present data set). Note that this method only calculates the gradient over a window of 10 km and thus it smoothens the sharpest density gradients at smaller scales. Small-scale electron density fluctuations tend to occur on the intermediate-scale density gradients. To present the relationship between density gradients and small-scale density fluctuations, we choose the locations of peaks and valleys of ∇Ne that show at least a magnitude of 1.5×10^3 cm^{-3}/km. This threshold is chosen to balance the statistical significance with enough data points and the event significant with sharpest density gradients. The peaks and valleys are shown as magenta dots and blue triangles in Figure 1e, respectively. In total, 10 positive and 10 negative gradients are selected. Near the peaks and valleys of density gradients, we calculate the upper quartile of RMS Ne in a window of 3 km centered at the peak gradients. Figure 2 presents the results in a scatter plot. The small-scale density fluctuations are correlated with electron density gradients. A linear fit of the gradients and RMS Ne are presented as dashed lines for both positive and negative gradients. Unlike the scenario in Moen et al. (2012), we don't see a clear enhancement in small-scale density fluctuations with a preference for either negative or positive gradients. This indicates a symmetric growth of small-scale irregularities on both edges.

3.2. Event on November 4, 2017

Due to the displacement between the magnetic and geographic poles in the Northern Hemisphere, NorSat-1 does not fly in the noon-midnight magnetic meridian and the maximum latitude is ∼80° MLAT between 17 UT and 03 UT. For these orbits, NorSat-1 often intersects auroral precipitation region in the dawnside when the dawnside auroral oval is thick or when the auroral oval is contracted during northward interplanetary magnetic field and low magnetic activity. In addition, polar cap arcs were also often observed in the dawnside polar cap (not shown in the present paper) (Zhu et al., 1997). This is often the case during the current solar minimum. We will now present a case of the dawnside aurora. Figure 3a shows the auroral

Figure 1. (a) An auroral image at Lyman-Birge-Hopfield long (LBHL) band from Special Sensor Ultraviolet Spectrographic Imager (SSUSI) onboard Defense Meteorological Satellite Program (DMSP) F18. (b) The Global Positioning System (GPS) Total Electron Content (TEC) map in the northern hemisphere. Both maps are presented in Magnetic LATitude (MLAT)/Magnetic Local Time (MLT) coordinates, where magnetic noon is to the top and dawn in on the right. In panel a, the orbits of F18 and NorSat-1 are presented as black and red lines with timestamps annotated. The Feldstein auroral oval is shown as magenta circle for $Q = 3$ (Holzworth & Meng, 1975). The solar terminator is shown as a gray line. (c) The electron density observed by the NorSat-1 satellite. (d) The expanded version of the electron density to present the region of enhanced density fluctuations. (e) The density gradient in a running window of 10 km is shown in as red, while the root mean square (RMS) of electron density in running window of 50 m is shown as black. The magenta dots and blue triangles mark the locations of the peak positive and negative density gradients.
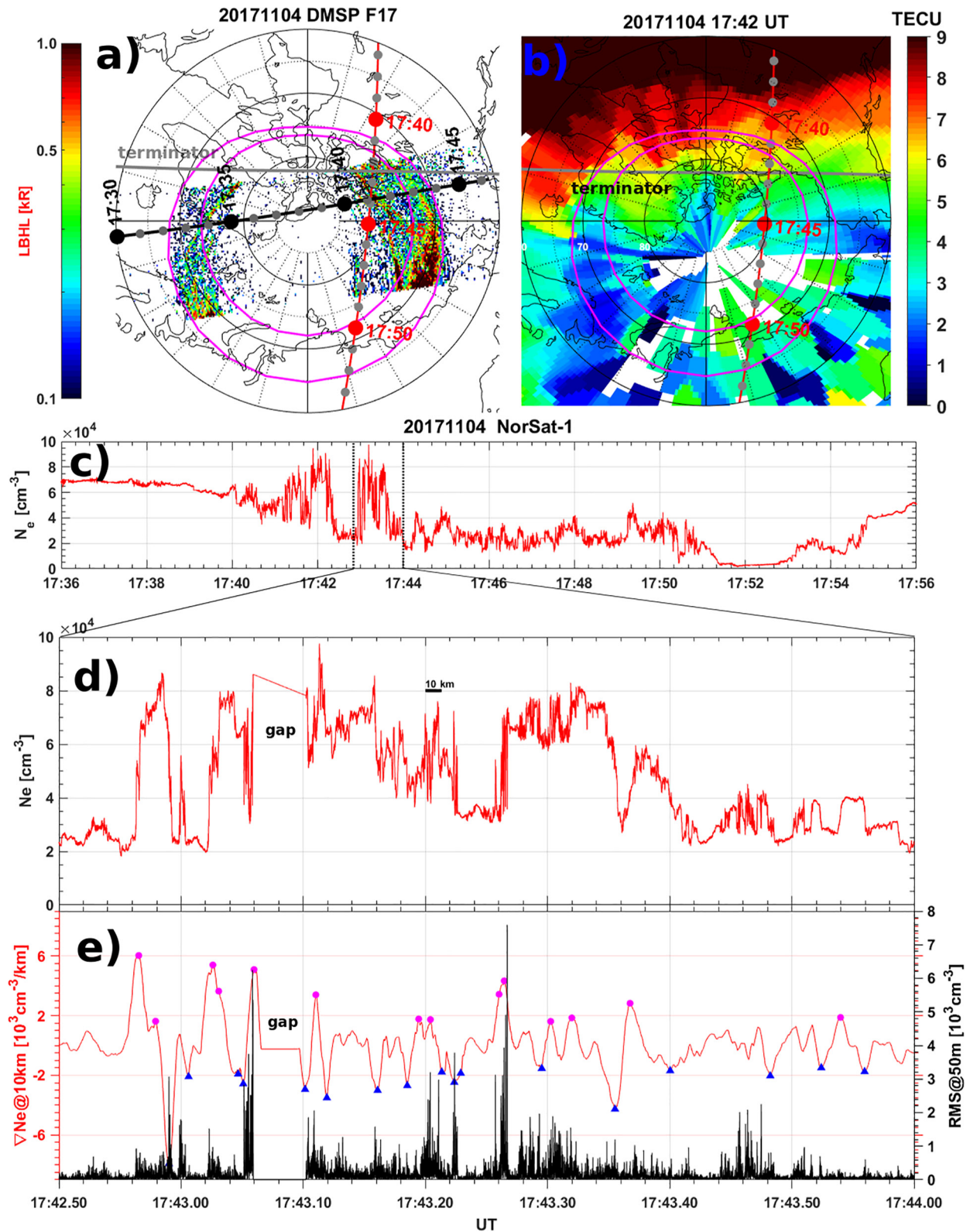
Figure 3. The same format as Figure 1, but for November 4, 2017 in the dawnside aurora. The scatter plot of peak density gradients (magenta dots and blue triangles) and Ne root mean square (RMS) corresponding to panel (e) can be found in the Supporting Information S1.

image at LBHL band by DMSP F17. Unfortunately, the field-of-view of SSUSI could not cover the dayside aurora completely. However, based on the DMSP SSUSI auroral image, NorSat-1 entered the auroral zone at ~17:41 UT and remained in the auroral zone until at least 17:48 UT (cf., Figure 3a). The solar terminator was poleward of the dayside auroral oval. Because of this, there were some intrusions of dense dayside photo-ionized plasma into the polar cap following the high-latitude convection as seen from the GPS TEC map from Figure 3b.

Figure 3c presents the electron density from the m-NLP. The electron density is derived from probes #2, #3, and #4. The Langmuir probes were biased to 6, 7.5, and 9 V, respectively. On this day, the sampling frequency was 400 Hz. There were three periods with large-scale electron density enhancements during 17:41–17:44 UT. Figures 3d and 3e show the third region of density enhancement during 17:42.50–17:44 UT. Clearly, there were small-scale density fluctuations along the edges of the intermediate-scale density enhancements, especially near 17:43.30 UT. This is similar to the case in Section 3.1. The scatter plot of peak density gradients and Ne RMS corresponding to Figure 3e can be found in the Supporting Information S1.

3.3. Statistics

We will now present statistical results based on data from the NorSat-1 satellite. We make use of the data during November and December of 2017. During this time period, the sampling rate was varied between 400 Hz and 1 kHz. The different sampling rates should not affect the statistics as we are considering spatial scales of 10, 500, and 50 m, which correspond to temporal scales of 0.75, 15, and 150 Hz, respectively. These scales are well inside the lowest sampling rates of 400 Hz. For this statistical study, we have visually checked the data quality and manually masked out orbits with significant number of erroneous measurements. These are seen as the electric current collapsing to nearly zero for all four Langmuir probes and when the linearity of squared currents used for retrieving plasma density is very low (below 0.5). These erroneous data can be caused by spacecraft charging in the Earth shadow or attitude control (Ivarsen et al., 2019). Furthermore, the mNLP system cannot always be run continuously. Due to the high temporal resolution of four probes, the obtained data are quite big. However, the speed for downloading the data from the NorSat-1 downlink antenna is limited. In total, 220 out of 243 orbits are used to construct the statistics. In addition, we only use data when the linearity of the three Langmuir probes is above 0.8 (Hoang et al., 2018). The dates of the measurements and data resolution can be found in the Supporting Information S2.

We choose to show the statistics based on four parameters, namely the electron density, density gradients over 10 km, RMS of Ne over 500 m and RMS of Ne over 50 m. The data are binned in equal-area cells in MLAT and MLT (Jin et al., 2019). Each cell is approximately 200 × 400 km (about 2° in latitude × 4° in longitude at the equator).

Due to the orbit of NorSat-1, the data only cover part of the high-latitude ionosphere in magnetic coordinates. The Feldstein auroral oval is also plotted to assist the analysis (Holzworth & Meng, 1975). This parameter $Q = 2$ is chosen to match the average Kp index during the period (Kp ∼ 1.7). The pattern of the electron density is similar to the one obtained using the in-situ data from the Swarm satellites (Jin et al., 2019) and it can be explained by the solar illumination and high-latitude auroral dynamics. The electron density is clearly enhanced on the dayside, consistent with solar EUV illumination (the solar terminator is presented as gray line). Furthermore, there is a clear density enhancement near 75°–80° MLAT near 12 MLT. This is likely due to soft particle precipitation in the cusp region. Figure 4b shows that the intermediate-scale density gradients are enhanced in the cusp region, similar to the electron density. Figures 4c and 4d present small-scale density fluctuations at 500 and 50 m, respectively. The small-scale density fluctuations are also enhanced in and slightly poleward of the cusp region. In addition, there are several cells with enhanced small-scale density fluctuations in the dawnside near 75°–80° MLAT. Compared to the dayside, Figure 4 shows that on average the nightside ionosphere is relatively unstructured. The electron density and RMS Ne are not clearly enhanced in the nightside auroral oval. However, there are sporadic enhancements of intermediate-scale density gradients in the nightside auroral oval as shown in Figure 4b.
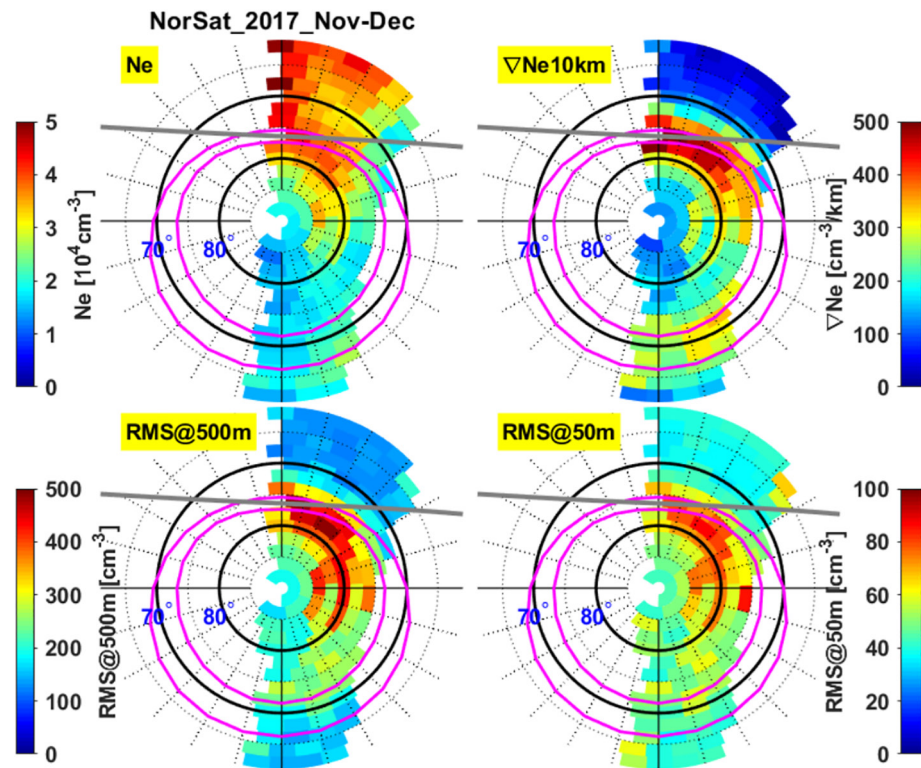
Figure 4. The mean electron density (a), density gradients in 10 km scale (b), root mean square (RMS) in 500 m scale (c) and RMS of Ne in 50 m scale (d) in Magnetic LATitude (MLAT)/Magnetic Local Time (MLT) coordinates using data from NorSat-1. In panel (b), we use the absolute value of density gradients to construct the statistics. In each panel, MLT noon is to the top and dawn is to the right. The MLAT of 70° and 80° are shown by solid black lines. The Feldstein oval is plotted as magenta curves as a reference for the statistical location of the auroral oval. The gray line in each panel presents the solar terminator, which is calculated at 17 UT on November 30, 2017.

4. Summary and Discussion

In this study, we have presented two cases of high-resolution electron density fluctuations during the passes through noon-time cusp aurora and the dawnside aurora. Then we have shown the statistical distribution of intermediate-scale density gradients at 10 km and small-scale irregularities at scales of 50 and 500 m. This is the first time such a statistical map of plasma irregularities at decameter scales has been presented using in-situ technique. To obtain the variations at different scales, we assume that the observed plasma irregularities are spatial rather than temporal. This is a reasonable assumption, as the plasma is moving much slower than the spacecraft.

NorSat-1 was operated during low solar activity (routine operation started only after November 2017) and the attitude control was not stable after May 2018. For the data we have, we did not observe many classical polar cap patches that are formed from the photo-ionized plasma in the sunlit ionosphere, while significant plasma irregularities have been observed in the auroral zone (either cusp or the dawnside aurora). In the previous in-situ studies of high-latitude plasma structures, it has been shown that plasma density enhancements are often unstable on the trailing edge and stable on the leading edge, such that small-scale irregularities are only associated with one side of density gradients (Cerisier et al., 1985; Moen et al., 2012; Spicher et al., 2015). As a result, the GDI is thought to be the main source mechanism for the development of small-scale irregularities (Tsunoda, 1988). In the current study, however, we cannot see a clear preference of small-scale irregularities over positive gradients nor negative gradients. For the two cases we presented, the small-scale irregularities can be found on both positive and negative gradients. As NorSat-1 travels from the dayside to the nightside, a positive gradient indicates an anti-sunward density gradient. When a plasma structure drifts anti-sunward (such as the case in Figure 1), a positive density gradient would indicate the growth of GDI. The scenario is more complex for northward interplanetary magnetic field, during which

the plasma could drift in the sunward direction. The drift motion of the high-latitude plasma structures is quite pulsed and dynamical (Oksavik et al., 2010). The history of motion of a density gradient is important for the growth of plasma irregularities. For example, Gondarenko et al. (2003) simulated the operation of GDI with a plasma patch under a variable E × B drift. In that scenario, plasma structuring could be found on both edges of the plasma patch because of occasional reversal of the drift direction. Additionally, for a circular polar cap patch (in contrast to traditional simulations where only leading and trailing edges are considered (e.g., Gondarenko et al., 2003)), irregularity growth can occur on all edges except for the one point where the density gradient is antiparallel to the drift velocity (Lamarche et al., 2020).

The results show that there is a positive correlation between intermediate-scale density gradients and small-scale irregularities for both positive and negative gradients. This indicates that turbulence mixing driven by AC electric field may also play a role in developing small-scale irregularities as this mechanism is independent on the direction of density gradients (Burston et al., 2016; Kelley, 2009). Additional physical mechanisms can complicate the scenario further. For example, as the plasma structures were observed in the auroral zone, particle precipitation and field-aligned (Birkeland) currents could drive the stable gradients unstable by the current convective instability (Ossakow & Chaturvedi, 1979). Clausen et al. (2016) demonstrated that GPS phase scintillations are strongest underneath the upward currents of the region 1/region 2 field aligned current system. In addition, the auroral structures are often associated with flow shears, and then the Kelvin-Helmholtz instability (KHI) and the subsequent inhomogeneous energy-density-driven instability (IEDDI) can operate as a process to create small-scale irregularities (Spicher et al., 2016). There is a need for observations of other key physical parameters (e.g., particle precipitation, plasma velocities, field-aligned currents, and AC electric field) to be able to rule out the contribution from other source mechanisms such as the current convective instability (Ossakow & Chaturvedi, 1979), KHI (Keskinen & Ossakow, 1983; Keskinen et al., 1988) and turbulence mixing (Kelley, 2009).

Traditionally, the statistics of decameter ionospheric irregularities have been investigated using remote sensing from HF radars (e.g., Ghezelbash, 2013; Ghezelbash et al., 2014). The spatial distribution of decameter scale irregularities in Figure 4 is similar to the occurrence of HF backscatter echoes in a recent study using the HF radars at Rankin Inlet and Inuvik (see Figure 4.2 in Ghezelbash, 2013). The Rankin Inlet radar data cover all local times for magnetic latitudes above 75°. For the area with common field-of-view, both backscatter echoes and Ne RMS show enhancements around the cusp and in the dawnside sector at MLAT 75°–80°. However, the averaged Ne RMS in the nightside ionosphere is relatively low as compared to the HF backscatter echoes. This is probably due to different statistical methods and it will be investigated in a dedicated future work. In Figure 4, we calculate the mean values of Ne RMS, while most of the studies of HF backscatter use occurrence rate of the HF echoes as a measure of decameter irregularities. Jin et al. (2015), with a GPS scintillation study that observes ionospheric irregularities at intermediate scales (∼km), show that different thresholds of the GPS phase scintillation index could change the day/night contrast of scintillation occurrences, that is, strong scintillations tend to occur in the nightside ionosphere while there are high occurrence rates of weak scintillations in the dayside ionosphere. This feature also applies for the decameter scale irregularities. Although focusing at different scales, the results are also similar to the distribution of GPS signal losses onboard the Swarm satellite (Xiong et al., 2018). The GPS signal losses happen when Swarm encounters large amplitude density gradients. This also suggests the multi-scale characteristics of the high-latitude ionosphere and the coexistence of ionospheric irregularities at a broad scale range.

With the current in-situ data, we could not directly measure plasma irregularities at 15 m scale. This is because NorSat-1 uses a low-pass filter to eliminate high-frequency noise before using the Analog-to-Digital converter. The highest unaffected frequency after the low-pass filter is about 333 Hz (corresponding to 22.5 m in spatial scale). In order to directly compare the HF backscatter at 10 m scale with in-situ electron density irregularities by the AUREOL-3 satellite, Villain et al. (1986) extrapolated the power spectra density from 40 to 10 m by using the spectral slope obtained from 10 km to 40 m. Though satisfactory results have been obtained, the uncertainty is still significant: that is, the deviation of 1 in the spectral slope can lead to an error of a factor 4 on the power spectra (Villain et al., 1986). In a conjunction event between NorSat-1 and the Longyearbyen HF radar, Lie (2019) found enhanced density fluctuations at ∼15 m scale for the case with good HF backscatter despite the low pass filter at 333 Hz for the NorSat-1 data. This indicates that it

is now possible to directly compare in-situ ionospheric irregularities with HF backscatter data, which is a natural step in future analyses.

5. Conclusion

The ionospheric irregularities are not only associated with anti-sunward (positive) density gradients, indicating that the GDI is not the only seed mechanism for polar ionospheric irregularities. The statistical distribution of decameter scale (50 m) ionospheric irregularities is aligned with the auroral oval, as did the statistical distribution of GPS scintillations at high latitudes (Clausen et al., 2016). This indicates that major part of the plasma irregularities in the polar ionosphere is driven by auroral dynamics, and that there are many candidate instability mechanisms. The NorSat-1 data are now openly available http://tid.uio.no/plasma/norsat/. Due to the significantly high-resolution sampling (up to 1 kHz as compared to the 2 Hz electron density data from Swarm satellites (Knudsen et al., 2017)), NorSat-1 provides a new opportunity in studies of the multi-scale structures and dynamics in the ionosphere. The satellite routinely crosses the equatorial and polar regions twice every 90 min, thus it provides a wealth of unique data that can improve our understanding about the mechanisms that dissipate energy input at larger scales by creating small-scale plasma density structures within the ionosphere. We believe that the high-resolution in-situ data will help to better understand the dynamics and nature of small-scale irregularities (especially from sub-km to decameter scales).

Data Availability Statement

The GPS TEC data for GPS TEC map can be obtained through the Madrigal database (http://cedar.openmadrigal.org/ftp/fullname/Yaqi+Jin/email/yaqi.jin@fys.uio.no/affiliation/Universitetet+i+Oslo/kinst/8000/year/2017/kindat/3500/format/hdf5/). The NorSat-1 data can be obtained through http://tid.uio.no/plasma/norsat/. The DMSP SSUSI data were obtained from The Johns Hopkins University Applied Research Laboratory (https://ssusi.jhuapl.edu/data_retriver?spc=f17&type=edr-aur&year=2017&Doy=308 and https://ssusi.jhuapl.edu/data_retriver?spc=f18&type=edr-aur&year=2017&Doy=334).

References

Baker, K., Greenwald, R., Walker, A., Bythrow, P., Zanetti, L., Potemra, T., et al. (1986). A case study of plasma processes in the dayside cleft. *Journal of Geophysical Research*, *91*(A3), 3130–3144. https://doi.org/10.1029/JA091iA03p03130

Bekkeng, T. A., Jacobsen, K. S., Bekkeng, J. K., Pedersen, A., Lindem, T., Lebreton, J. P., & Moen, J. I. (2010). Design of a multi-needle Langmuir probe system. *Measurement Science and Technology*, *21*(8). https://doi.org/10.1088/0957-0233/21/8/085903

Burston, R., Mitchell, C., & Astin, I. (2016). Polar cap plasma patch primary linear instability growth rates compared. *Journal of Geophysical Research: Space Physics*, *121*(4), 3439–3451. https://doi.org/10.1002/2015JA021895

Cerisier, J. C., Berthelier, J. J., & Beghin, C. (1985). Unstable density gradients in the high-latitude ionosphere. *Radio Science*, *20*(4), 755–761. https://doi.org/10.1029/RS020i004p00755

Clausen, L. B. N., Moen, J. I., Hosokawa, K., & Holmes, J. M. (2016). GPS scintillations in the high latitudes during periods of dayside and nightside reconnection. *Journal of Geophysical Research: Space Physics*, *121*(4), 3293–3309. https://doi.org/10.1002/2015ja022199

Ghezelbash, M. (2013). *Occurrence and causes of F-region echoes for the Canadian PolarDARN/SuperDARN radars*. University of Saskatchewan.

Ghezelbash, M., Koustov, A. V., Themens, D. R., & Jayachandran, P. T. (2014). Seasonal and diurnal variations of PolarDARN F region echo occurrence in the polar cap and their causes. *Journal of Geophysical Research: Space Physics*, *119*, 426–410. https://doi.org/10.1002/2014ja020726

Gondarenko, N. A., Guzdar, P. N., Sojka, J. J., & David, M. (2003). Structuring of high latitude plasma patches with variable drive. *Geophysical Research Letters*, *30*(4), 1165. https://doi.org/10.1029/2002gl016437

Hoang, H., Clausen, L. B. N., Roed, K., Bekkeng, T. A., Trondsen, E., Lybekk, B., et al. (2018). The multi-needle Langmuir probe system on board NorSat-1. *Space Science Reviews*, *214*(4). https://doi.org/10.1007/s11214-018-0509-2

Holzworth, R. H., & Meng, C. I. (1975). Mathematical representation of auroral oval. *Geophysical Research Letters*, *2*(9), 377–380. https://doi.org/10.1029/GL002i009p00377

Ivarsen, M. F., Hoang, H., Yang, L., Clausen, L. B., Spicher, A., Jin, Y., et al. (2019). Multineedle langmuir probe operation and acute probe current susceptibility to spacecraft potential. *IEEE Transactions on Plasma Science*, *47*(8), 3816–3823.

Jacobsen, K. S., Pedersen, A., Moen, J. I., & Bekkeng, T. A. (2010). A new Langmuir probe concept for rapid sampling of space plasma electron density. *Measurement Science and Technology*, *21*(8), 085902. https://doi.org/10.1088/0957-0233/21/8/085902

Jin, Y. Q., Moen, J. I., & Miloch, W. J. (2015). On the collocation of the cusp aurora and the GPS phase scintillation: A statistical study. *Journal of Geophysical Research: Space Physics*, *120*(10), 9176–9191. https://doi.org/10.1002/2015ja021449

Jin, Y. Q., Spicher, A., Xiong, C., Clausen, L. B. N., Kervalishvili, G., Stolle, C., & Miloch, W. J. (2019). Ionospheric plasma irregularities characterized by the swarm satellites: Statistics at high latitudes. *Journal of Geophysical Research: Space Physics*, *124*(2), 1262–1282. https://doi.org/10.1029/2018ja026063

Kelley, M. C. (2009). *The earth's ionosphere: Plasma physics and electrodynamics*. Academic press.

Kelley, M. C., Vickrey, J. F., Carlson, C. W., & Torbert, R. (1982). On the origin and spatial extent of high-latitude F-region irregularities. *Journal of Geophysical Research*, *87*, 4469–4475. https://doi.org/10.1029/JA087iA06p04469

Keskinen, M. J., Mitchell, H. G., Fedder, J. A., Satyanarayana, P., Zalesak, S. T., & Huba, J. D. (1988). Nonlinear evolution of the kelvin-helmholtz instability in the high-latitude ionosphere. *Journal of Geophysical Research*, *93*(A1), 137–152. https://doi.org/10.1029/JA093iA01p00137

Keskinen, M. J., & Ossakow, S. L. (1983). Theories of high-latitude ionospheric irregularities — A review. *Radio Science*, *18*(6), 1077–1091. https://doi.org/10.1029/RS018i006p01077

Knudsen, D. J., Burchill, J. K., Buchert, S. C., Eriksson, A. I., Gill, R., Wahlund, J. E., et al. (2017). Thermal ion imagers and Langmuir probes in the Swarm electric field instruments. *Journal of Geophysical Research: Space Physics*, *122*(2), 2655–2673. https://doi.org/10.1002/2016ja022571

Labelle, J., Sica, R. J., Kletzing, C., Earle, G. D., Kelley, M. C., Lummerzheim, D., et al. (1989). Ionization from soft electron-precipitation in the auroral F-region. *Journal of Geophysical Research*, *94*(A4), 3791–3798. https://doi.org/10.1029/JA094iA04p03791

Lamarche, L. J., Varney, R. H., & Siefring, C. L. (2020). Analysis of plasma irregularities on a range of scintillation-scales using the resolute bay incoherent scatter radars. *Journal of Geophysical Research: Space Physics*, *125*(3), e2019JA027112. https://doi.org/10.1029/2019JA027112

Lie, H. B. (2019). Master Thesis *Decameter scale irregularities in the polar ionosphere*. University of Oslo. Retrieved from https://www.duo.uio.no/handle/10852/71421

Milan, S. E., Yeoman, T. K., Lester, M., Thomas, E. C., & Jones, T. B. (1997). Initial backscatter occurrence statistics from the CUTLASS HF radars. *Annales Geophysicae-Atmospheres Hydrospheres and Space Sciences*, *15*(6), 703–718. https://doi.org/10.1007/s00585-997-0703-0

Moen, J., Oksavik, K., Abe, T., Lester, M., Saito, Y., Bekkeng, T. A., & Jacobsen, K. S. (2012). First in-situ measurements of HF radar echoing targets. *Geophysical Research Letters*, *39*, L07104. https://doi.org/10.1029/2012gl051407

Oksavik, K., Barth, V. L., Moen, J., & Lester, M. (2010). On the entry and transit of high-density plasma across the polar cap. *Journal of Geophysical Research*, *115*, A12308. https://doi.org/10.1029/2010ja015817

Ossakow, S. L., & Chaturvedi, P. K. (1979). Current convective instability in the diffuse aurora. *Geophysical Research Letters*, *6*(4), 332–334. https://doi.org/10.1029/GL006i004p00332

Paxton, L. J., Morrison, D., Zhang, Y. L., Kil, H., Wolven, B., Ogorzalek, B. S., et al. (2001). Validation of remote sensing products produced by the Special Sensor Ultraviolet Scanning Imager (SSUSI) - A far-UV imaging spectrograph on DMSP F16. *Optical Spectroscopic Techniques Remote Sensing, and Instrumentation for Atmospheric and Space Research Iv*, *4485*, 338–348. https://doi.org/10.1117/12.454268

Rideout, W., & Coster, A. (2006). Automated GPS processing for global total electron content data. *GPS Solutions*, *10*(3), 219–228. https://doi.org/10.1007/s10291-006-0029-5

Ruohoniemi, J. M., & Greenwald, R. A. (1997). Rates of scattering occurrence in routine HF radar observations during solar cycle maximum. *Radio Science*, *32*(3), 1051–1070. https://doi.org/10.1029/97rs00116

Spicher, A., Cameron, T., Grono, E. M., Yakymenko, K. N., Buchert, S. C., Clausen, L. B. N., et al. (2015). Observation of polar cap patches and calculation of gradient drift instability growth times: A Swarm case study. *Geophysical Research Letters*, *42*(2), 201–206. https://doi.org/10.1002/2014gl062590

Spicher, A., Ilyasov, A. A., Miloch, W. J., Chernyshov, A. A., Clausen, L. B. N., Moen, J. I., et al. (2016). Reverse flow events and small-scale effects in the cusp ionosphere. *Journal of Geophysical Research-Space Physics*, *121*(10), 10466–10480. https://doi.org/10.1002/2016ja022999

Tsunoda, R. T. (1988). High-latitude F-region irregularities — A review and synthesis. *Reviews of Geophysics*, *26*(4), 719–760. https://doi.org/10.1029/RG026i004p00719

Villain, J., Hanuise, C., & Beghin, C. (1986). *ARCAD 3-SAFARI coordinated study of auroral and polar F-region ionospheric irregularities*. Paper presented at the Annales Geophysicae.

Xiong, C., Stolle, C., & Park, J. (2018). Climatology of GPS signal loss observed by Swarm satellites. *Annales Geophysicae*, *36*(2), 679–693. https://doi.org/10.5194/angeo-36-679-2018

Zhu, L., Schunk, R. W., & Sojka, J. J. (1997). Polar cap arcs: A review. *Journal of Atmospheric and Solar-Terrestrial Physics*, *59*(10), 1087–1126. https://doi.org/10.1016/S1364-6826(96)00113-7